Ti6Al4V Components by Bound Metal Deposition and Competitive with Metal Injection Molded Parts: Optimization of the Printing Parameters

Published Version:
Sergi, C., Martucci, A., Galati, M., Lombardi, M., Rossi, E., Sebastiani, M., et al. (2025). Ti6Al4V Components by Bound Metal Deposition and Competitive with Metal Injection Molded Parts: Optimization of the Printing Parameters. ADVANCED ENGINEERING MATERIALS, 27(10), 1-18 [10.1002/adem.202402813].

Published:
DOI: http://doi.org/10.1002/adem.202402813

Claudia Sergi*, Alessandra Martucci, Manuela Galati, Mariangela Lombardi, Edoardo Rossi, Marco Sebastiani, Lavinia Tonelli, Lorella Ceschini, Jacopo Tirillò, Fabrizio Sarasini

Ti6Al4V Components by Bound Metal Deposition and Competitive with Metal Injection Molded Parts: Optimization of the Printing Parameters

In: Adv. Eng. Mater. 2025, 27, 2402813

https://doi.org/10.1002/adem.202402813

Ti6Al4V Components By Bound Metal Deposition And Competitive With Metal Injection Molded Parts: Optimization Of The Printing Parameters

Claudia Sergi[1*], Alessandra Martucci[2], Manuela Galati[3,4], Mariangela Lombardi[2], Edoardo Rossi[5], Marco Sebastiani[5], Lavinia Tonelli[6], Lorella Ceschini[6], Jacopo Tirillò[1], Fabrizio Sarasini[1]

[1]Department of Chemical Engineering Materials Environment, Sapienza Università di Roma and UdR INSTM, Via Eudossiana 18, 00184, Rome, Italy
[2] Department of Applied Science and Technology, Politecnico di Torino, Corso Duca Degli Abruzzi 24, 10129, Turin, Italy
[3] Department of Management and Production Engineering, Politecnico di Torino, Corso Duca Degli Abruzzi 24, 10129, Turin, Italy
[4] Integrated Additive Manufacturing Center, Politecnico di Torino, Corso Duca Degli Abruzzi 24, 10129, Turin, Italy
[5] Department of Civil, Computer Science and Aeronautical Technologies Engineering, Roma Tre University, Via Vito Volterra 62, 00146 Rome, Italy
[6] Department of Industrial Engineering (DIN), Alma Mater Studiorum—University of Bologna, Viale del Risorgimento 2, 40136 Bologna, Italy

*Corresponding author: claudia.sergi@uniroma1.it

ABSTRACT

Bound Metal Deposition (BMD) is a valid 3D printing solution from an economic perspective. Still, the resulting mechanical properties are intrinsically lower than Selective Laser Melting (SLM) and Electron Beam Melting (EBM) ones and, in some cases, are also lower than MIM (Metal Injection Molding). The optimization of the printing parameters is fundamental to level off this issue and to ensure mechanical performance competitive with MIM ones. In light of this, the present work focused, for the first time, on the optimization of the printing parameters for a Ti6Al4V alloy. The effect of three fundamental parameters, i.e., layer thickness, nozzle temperature, and printing speed, was investigated and the 3D printing process was optimized by exploiting the Design of Experiment (DoE) and the surface response analysis techniques. The results are extremely auspicious, considering that the optimum configurations displayed a tensile strength of 915 MPa, which is perfectly comparable with MIM components. The statistical analysis demonstrated that nozzle temperature, printing speed, and their interaction, are the most relevant parameters and the 3D printing optimum is achieved with a nozzle temperature of 160 °C and a printing speed of 15 mm/s.

Keywords: Ti6Al4V alloy, Bound Metal Deposition, Design of Experiment, Nano Indentation, micro-CT

1 INTRODUCTION

Industry 4.0 represents a new manufacturing paradigm where the interconnectivity among human operators, machines, and computers ensures improved manufacturing efficiency, larger production scales, and an improved life quality [1]. Among the innovative technologies which allowed the development of this new manufacturing revolution, e.g., Internet of Things, Artificial Intelligence, machine learning, big data, and augmented reality, a significant contribution was provided by additive manufacturing (AM), which enabled and enhanced a new commercial approach, i.e., Mass Customization [2]. Indeed, among all AM advantages, e.g., waste minimization, higher freedom of design and fast prototyping [3], product customization plays a pivotal role enabling the manufacturing of products tailored to consumer needs and desires while maintaining a good manufacturing speed and efficiency.

This design and manufacturing flexibility are of paramount importance in key industrial sectors such as aerospace [4] and transportation [5–7], where the design of optimized and lighter metal components through topological optimization and generative design [8] can significantly reduce the overall weight of the vehicles and the related fuel consumption with beneficial outcomes in terms of environmental impact [9]. Several technologies, such as powder bed fusion technologies with laser (PBF-LB) and electron beam (PBF-EB), direct energy deposition (DED), and binder jetting (BJT), are already available for metal 3D printing [10,11], but the high investment costs of purchasing the printing apparatus and the high operating costs resulting from the use of controlled atmospheres, e.g., vacuum or inert, and high energy sources tend to restrict their use only in those fields where a reasonable return on investment is expected.

Bound Metal Deposition (BMD), i.e., a polymer-based AM technique, was developed to overcome this issue. A green component is 3D printed with a fused filament fabrication (FFF) printer starting from a polymeric filament highly filled with metal powders and it is then subjected to debinding and sintering processes to obtain the final dense metallic part [12]. Considering that the investment costs related to FFF printers can be as low as 2,000 $ - 15,000 $ [13] while the costs of PBF techniques can reach 1 M$ [14], this manufacturing path is particularly appealing for all those companies that already produce components by metal injection molding (MIM) and already own debinding and sintering ovens. Indeed, the exploitation of BMD would ensure all the advantages connected with AM while keeping low the investment costs.

BMD compares favorably from an economic perspective even with binder jetting, i.e., another 3D printing technique which needs a debinding and sintering post processing to achieve the densification of the green 3D printed component. Even if, binder jetting ensures high build rates and large build volume [15], the investment costs related to the 3D printer are still higher than FFF ones, with prices ranging from 30,000 $ for basic machines up to 250,000 $ for large-scale and industrial-style printers [16,17].

If BMD appears to be a valid 3D printing solution from an economic perspective, it must be also considered that the resulting mechanical properties are intrinsically lower than the ones achievable by SLM and EBM due to the use of sintering as post-processing densification strategy, which entails the inherent presence of a residual porosity inside the metal part [18]. In light of this, the mechanical properties of BMD components and the final industrial applications expected for them are usually compared with the ones of MIM components since the post process of both techniques involves the same steps [19].

Indeed, MIM is a manufacturing process which enables the production of small-to-medium-sized precision components and present a cost-effective alternative to more traditional techniques, particularly for large production of complex-shaped parts [20,21]. For example, in the biomedical field, metallic implants are usually manufactured using ingot metallurgy, which involves casting semi-finished components which are subsequently subjected to further cold or hot working to improve mechanical properties, as well as to mechanical machining to reach the final net shape. This multi-step approach significantly increases the overall manufacturing costs [21]. MIM has also the paramount advantage to allow to produce cost-effective and complex shaped parts using almost all types of metals and intermetallic compounds [20].

MIM was developed by combining plastic injection molding and traditional powder metallurgy. Indeed, the first step of the manufacturing process, i.e., the shaping step, is similar to plastic injection molding, in which a polymeric binder is mixed with metal powders, heated, and injected into a mold cavity to achieve the desired shape. The second step referred to as the densification step, follows the principles of powder metallurgy wherein the polymer is removed via debinding, and the component is densified through sintering[20,22,23]. However, the manufacturing of components using titanium alloys is challenging due to the high affinity of titanium for oxygen.

Analogously, BMD was developed by combining plastic 3D printing through FDM and powder metallurgy to obtain the dense metal part. The main difference between the two techniques lies in their scalability: MIM is tailored for mass production of identical parts [23] relying on costly, fixed-shape molds, while BMD allows to exploit the inherent advantages of AM, such as the greater design flexibility and product customization. Given the benefits of BMD and the relatively low investment required for FFF printers, BMD presents an attractive opportunity for companies already utilizing MIM, as they can expand their product portfolio while leveraging existing debinding and sintering infrastructures [24].

Despite a similar densification pathway, the mechanical properties of BMD parts are lower than MIM ones in many cases due to the presence of voids generated during deposition of adjacent layers [25]. In light of this, the optimization of the printing strategy and of the printing parameters is fundamental to level off this issue and to ensure mechanical performance competitive with MIM ones. For example, Tosto et al. [26] carried out the optimization of BMD printing parameters for a 316L stainless steel and achieved mechanical performance competitive with MIM ones with an increase of 10–12% in tensile strength and of 38–48% in tensile strain at break compared to the previous non-optimized work on the same alloy.

Thanks to high specific mechanical properties and excellent corrosion resistance, titanium and its alloy are widely used in many industrial fields such as the automotive, aerospace and biomedical ones [27] and Ti6Al4V is one of the most popular. Despite this, the number of works focused on the optimization of the BMD process for this alloy is quite scarce. In particular, some studies focused on the optimization of the polymeric feedstock [28] trying also to reduce its environmental impact by exploiting eco-friendly polymers such as polyethylene glycol (PEG) [29] and polylactic acid (PLA) [24], while other studies focused on the optimization of the sintering process by assessing the effect of time and temperature [30] and of the atmosphere [31], but none of them investigated the optimization of the 3D printing parameters which is a crucial aspect to reduce as much as possible the presence of voids between adjacent layers, as previously pointed out.

In light of this, the present work aims to bridge this gap of knowledge by investigating the effect of three fundamental printing parameters, i.e., layer thickness, nozzle temperature, and printing speed, and optimizing the 3D printing step by exploiting the Design of Experiment (DoE) and surface response analysis techniques. In particular, the tensile and flexural properties of the Ti6Al4V alloy were optimized by applying a 2-level full factorial design. The results obtained were correlated with sample microstructure by using X-ray diffraction (XRD), grain size analysis, electron backscattered diffraction (EBSD), scanning electron microscopy (SEM), micro-computed tomography (micro CT) and nanoindentation. A multi-scale characterization approach is essential, as it provides critical insights beyond mechanical properties. For example, nanoindentation and EBSD allow to unveil localized variations in hardness, modulus, grain orientation, and phase distribution which may potentially affect not only mechanical performance but also corrosion resistance, wear behavior, and fatigue life. These techniques ensure a deeper understanding of how microstructural features influence material behavior, contributing to more reliable optimization and process control, particularly in additive manufacturing, where small variations can significantly impact long-term performance and durability.

2 MATERIALS AND METHODS

2.1 Materials and samples production

Ti6Al4V dense specimens were manufactured through BMD by coupling FFF 3D printing with traditional debinding and sintering processes. The green specimens were 3D printed with the commercial polymeric filament Ti6Al4V FIL01A provided by Element 22 using a Voron V2.4 direct drive 3D printer equipped with a 0.6 mm nozzle. All specimens were 3D printed using a 100 % infill, a 60 °C bed temperature, a 30 mm/s retraction speed, and an oversizing factor of 20 % to account for shrinkage during debinding and sintering. The parameters selected to perform the 3D printing optimization are layer thickness, nozzle temperature, and printing speed whose values were varied on two levels according to a 2^3 full factorial design. In particular, 200 and 300 μm were selected as low and high levels for layer thickness, 140 and 160 °C as low and high levels for nozzle temperature, and 15 and 25 mm/s as low and high levels for printing speed. This resulted in eight different printing configurations summarized in Table 1. The green samples obtained from the eight configurations were debound and sintered in the same conditions according to the process parameters patented by Element 22 to which the 3D printing postprocessing was outsourced. The sintering process is performed at a low temperature, i.e., maximum 1100 °C, thus ensuring the achievement of a fine-grained structures [32]. An example of the final specimens obtained is given in Figure S1 of Supplementary Materials.

Table 1: Printing profiles obtained by applying the 2^3 full factorial design.

Printing profiles	Factors and Levels Thickness (µm)	Nozzle Temperature (°C)	Printing Speed (mm/s)
1	200	140	25
2	200	140	15
3	300	140	25
4	300	140	15
5	200	160	25
6	200	160	15
7	300	160	25
8	300	160	15

2.2 Microstructural characterization

XRD and EBSD (section 2.5) were used to analyze the crystalline phases present in the 3D printed sintered specimens. XRD was carried out on the outer surface of bending samples before testing with a Philips X'Pert PRO diffractometer using Cu Kα monochromatic radiation (40 kV and 40 mA), a step size of 0.02°, a time per step of 1 s, and collecting the spectra in the range of 2θ= 20–90°.

The grain size distribution of each configuration was also evaluated. After cutting the specimens with a diamond saw blade, they were embedded in the Epothin 2 bicomponent epoxy resin provided by Buehler using a 2:1 resin to hardener ratio, and 24 hours at room temperature were allowed to ensure resin hardening. Then samples were lapped and polished using the Mecatech 334 polishing machine by Presi employing a co-rotating mode for the plate and the carousel, a rotation speed of 150 rpm for the plate and 100 rpm for the carousel containing the specimens and an overall force of 0.3 DaN. The first lapping phase used sandpapers with progressive grits of 180, 400, 800, 1200, 2500 and 4000 were used. After that, specimens were polished with 9, 6 and 3 µm diamond polishing suspensions for twenty-minute cycles. The polished specimens were then subjected to chemical etching for 15 seconds in an aqueous solution with 45 wt.% of nitric acid and 10 wt.% of hydrofluoric acid. The etched specimens were analyzed with the optical microscope Leica DMI 5000, and the resulting images were processed using the ImageJ software to measure the area of 500 grains for each configuration.

MicroCT analysis was performed with an X-Ray CT scanner GE Phoenix v tome|x s applying a voltage of 210 kV, a current of 90 µA and a voxel size of 0.0259 mm. The 3D volume of each configuration was reconstructed using the VGStudio Max 3.4 software starting from the 1001 2D projections collected for each sample. The porosity analysis was carried out on a portion of the inner volume of the specimens with dimensions of 5 mm × 4 mm × 8 mm as shown in Figure S2 of Supplementary Materials. The porosity of all the samples has been analyzed using the defect analysis module of the software VGStudio Max 3 which provides a complete description of each detected pore and the statistic of all the measured pores. Two samples were tested for each printing configuration.

2.3 Mechanical characterization

The mechanical properties of Ti6Al4V dense specimens were evaluated through tensile and 3-point bending tests. Tensile tests were performed according to ASTM E8 on dog-bone shaped specimens with an overall length of 100 mm, a width of the gauge section of 6 mm, and a thickness of 6 mm in an Instron 5584 equipped with a 150 kN load-cell. Tests were performed in displacement control, with a test speed of 2 mm/min, a grip-to-grip separation of 50 mm, a preload of 2 MPa and a clip extensometer with a gauge length of 30 mm. Flexural properties were evaluated according to ASTM D790 carrying out three-point bending tests and using rectangular specimens with a length of 80 mm, a width of 10 mm, and a thickness of 5 mm and a Zwick/Roell Z010 universal testing machine equipped with a 10 kN load-cell. The tests were performed with a speed of 2 mm/min, a span length of 58 mm and a preload of 2 MPa. Three specimens were tested both in tension and bending for each printing configuration.

Finally, a surface fracture analysis of the tensile tested specimens was performed with a field-emission scanning electron microscope (FE-SEM) MIRA 3 by Tescan to disclose potential differences in densification, porosity, and printed-structure of the various configurations.

2.4 Statistical analysis

The data obtained from mechanical testing, i.e., flexural and tensile modulus and strength, were statistically analyzed with a two-step procedure. In the first step, the statistical significance of the three manufacturing parameters under consideration, i.e., layer thickness (t), printing speed (s) and nozzle temperature (T), was evaluated through inferential statistic to understand if they play a significant effect on the dependent variables, i.e., flexural and tensile modulus and strength. The analysis was performed through the R-studio software, applying the F-test (ANOVA) with a linear model which also accounts for manufacturing parameters interactions and adopting a p-value < 0.05 as statistically significant limit.

Once the relevant independent variables were identified, the mechanical properties data, i.e., the dependent variables, were processed with the software Matlab to conduct a Response Surface Analysis and identify the manufacturing parameters which maximize material mechanical performance. A linear approximation function which accounts also for manufacturing parameters interaction, was used as reported in Equation 1:

$$Y(s,T) = a + b\ \times s + c \times\ T + d \times Ts \qquad (1)$$

where Y is the mechanical property under consideration, T the nozzle temperature and s the printing speed.

2.5 Nanoindentation and EBSD analysis

Nanoindentation techniques were exploited to characterize samples heterogeneous structure. Both Continuous Stiffness Measurement (CSM) and high-speed nanoindentation mapping (HSNM) comprehensively map the mechanical properties across the polished cross-sections of the alloys and provide a detailed understanding of the microstructural variations throughout the sample [33].

CSM experiments were first conducted using a KLA Corp iNano nanoindenter in pseudo-displacement control, reaching a maximum depth of 500 nm. A 5 × 5 grid indentation matrix with 30 μm spacing was used to ensure a broader statistical representation of samples mechanical response. The measurements were conducted at a constant strain rate of 0.2 1/s, positioning the indentations approximately 200 μm from the sample cross-section edges and away from the microporosities. The indents were aligned parallel to the sample short edges, with the y-axis corresponding to the building direction and the x-axis to the printing direction, providing average values for the elastic modulus and the hardness at a depth of 400 nm. Tip calibration was performed before each grid indentation on a certified fused quartz reference following ISO 14577 standard.

The CSM load-displacement curves were also used to determine the target load for subsequent high-speed mapping with the nanoBlitz 3D feature of the iNano nanoindenter. This high-speed nanoindentation produced two-dimensional maps of hardness and elastic modulus at a target load of 1.5 mN resulting in an average penetration depth of 110 nm selected for high-resolution grain-level observations. Mapping covered a 200 μm × 600 μm area, with 100 points along the x-direction and 300 points along the y-direction for a total number of 30,000 indentations. Point spacing followed the standard 1/20th depth rule to maintain optimal resolution while preventing cross-correlation between indents. The high-speed maps, oriented similarly to the CSM grid, were obtained only for the two most representative samples from the studied population.

Data analysis pre-processing involved outlier removal to exclude indents on weak interfaces, defects, and porosities, which are common artifacts in BMD processes. This was achieved by filtering the modulus, hardness, and contact depth data based on threshold values set between 1.75 and 2.25 times the interquartile range for each distribution. A Gaussian Mixture Model (GMM) deconvolution was then applied to analyze the high-speed nanoindentation data [34]. The GMM approach, which models the data as a combination of multiple Gaussian distributions, was chosen due to the significant overlap in mechanical properties arising from different phases, grain orientations, and precipitates. The model parameters were optimized iteratively using the Expectation-Maximization (EM) algorithm. A GMM with three Gaussian distributions was used to capture material main mechanical phases and account for interfaces and noise.

In addition to the one-dimensional (1D) GMM deconvolution of modulus and hardness data, two-dimensional (2D) GMM clustering was also performed, combining modulus and hardness data simultaneously, offering a more holistic view of material mechanical characteristics. The 2D GMM was preferred over k-means, k-medoids, and DBSCAN due to its better handling of overlapping clusters and covariance structure. Z-score normalization was applied to standardize the data and cluster initialization was based on the 1D GMM results. A regularization value of 0.001 further improved the stability and robustness of the 2D clustering.

The same configurations subjected to high-speed nanoindentation mapping, i.e., C4 and C8, were also subjected to EBSD analysis to provide a better understanding of the results obtained thus ensuring a direct correlation between mechanical properties and material microstructure. The samples, polished according to the procedure reported in section 2.2, were further subjected to ion milling with the SEMPrep2 by Technoorg Linda for final polishing. Ion milling was performed with a 10 kV voltage and 3.5 mA current on rotating and tilted sample, for a total milling time of 15 min. Ion milled specimens were then covered with a copper tape to make them fully conductive, and the EBSD analysis was performed with a FE-SEM Mira3 by Tescan equipped with a high resolution EBSD detector Bruker Quantax EBSD System and applying a 20 kV voltage. For each sample, two maps were acquired, one at low magnification to achieve a good statistic on grain size and shape and one at high magnification to obtain a more detailed estimation on the phase distribution along the microstructure.

3 RESULTS AND DISCUSSION

3.1 Mechanical characterization and statistical analysis

Tensile and 3-point bending tests were performed on the eight configurations, and the resulting data in terms of stiffness and strength are reported in Figure 1. These data were analyzed through ANOVA F-test to evaluate the statistical significance of the printing parameters considered and their actual effect they played on Ti6Al4V mechanical response (Tables 2-5).

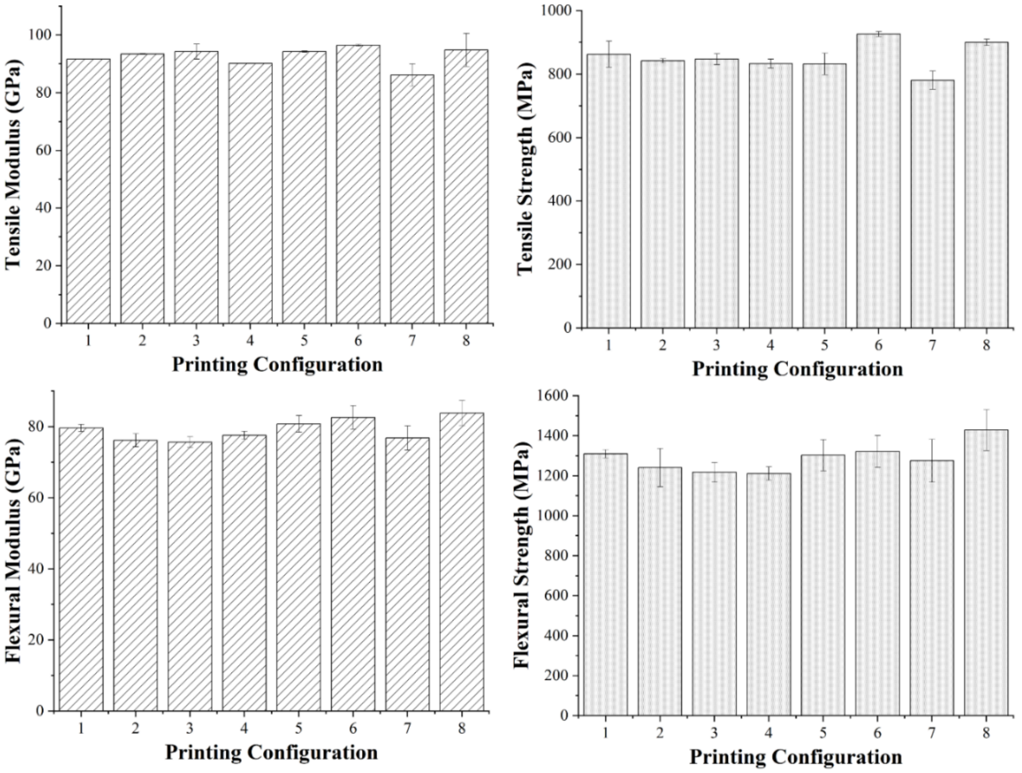

Figure 1: Average tensile and flexural modulus and strength values of the eight configurations with error bars representing the related standard deviation.

Table 2: Results of the ANOVA test to evaluate the statistical significance of the effects of the printing parameters, i.e., layer thickness, nozzle temperature and printing speed, and their interactions on samples tensile modulus. (R-squared = 0.55)

	Df	Sum Sq	Mean Sq	F Value	Pr(>F)	
Temperature	1	1.148	1.148	0.0885	0.769	
Thickness	1	28.188	28.188	2.171	0.158	
Speed	1	18.674	18.674	1.438	0.246	
Temperature:Thickness	1	0.315	0.315	0.024	0.878	
Temperature:Speed	**1**	**69.326**	**69.326**	**5.339**	**0.033**	*
Thickness:Speed	1	10.868	10.868	0.837	0.37	
Residuals	17	220.706	12.983			

Signif. codes: 0 ‘***’ 0.001 ‘**’ 0.01 ‘*’ 0.05 ‘.’ 0.1 ‘ ’ 1

Table 3: Results of the ANOVA test to evaluate the statistical significance of the effects of the printing parameters, i.e., layer thickness, nozzle temperature and printing speed, and their interactions on samples tensile strength. (R-squared = 0.81)

	Df	Sum Sq	Mean Sq	F Value	Pr(>F)	
Temperature	**1**	**1630.4**	**1630.4**	**3.467**	**0.079**	.
Thickness	**1**	**2466.7**	**2466.7**	**5.245**	**0.035**	*
Speed	**1**	**11180.6**	**11180.6**	**23.777**	**0.0001**	***
Temperature:Thickness	1	28.6	28.6	0.06	0.808	
Temperature:Speed	**1**	**18702.5**	**18702.5**	**39.774**	**7.885e-06**	***
Thickness:Speed	**1**	**1332.8**	**1332.8**	**2.834**	**0.015**	*
Residuals	17	7993.6	470.2			

Signif. codes: 0 ‘***’ 0.001 ‘**’ 0.01 ‘*’ 0.05 ‘.’ 0.1 ‘ ’ 1

Table 4: Results of the ANOVA test to evaluate the statistical significance of the effects of the printing parameters, i.e., layer thickness, nozzle temperature and printing speed, and their interactions on samples flexural modulus. (R-squared = 0.68)

	Df	Sum Sq	Mean Sq	F Value	Pr(>F)	
Temperature	**1**	**83.627**	**83.627**	**14.670**	**0.00134**	**
Thickness	1	10.402	10.402	1.824	0.194	
Speed	**1**	**20.167**	**20.167**	**3.537**	**0.077**	.
Temperature:Thickness	1	0.007	0.007	0.0012	0.973	
Temperature:Speed	**1**	**40.042**	**40.042**	**7.024**	**0.0168**	*
Thickness:Speed	**1**	**41.607**	**41.607**	**7.298**	**0.015**	*

Residuals	17	96.908	5.700			

Signif. codes: 0 ‘***’ 0.001 ‘**’ 0.01 ‘*’ 0.05 ‘.’ 0.1 ‘ ’ 1

Table 5: Results of the ANOVA test to evaluate the statistical significance of the effects of the printing parameters, i.e., layer thickness, nozzle temperature and printing speed, and their interactions on samples flexural strength. (R-squared = 0.54)

	Df	Sum Sq	Mean Sq	F Value	Pr(>F)	
Temperature	**1**	**45613**	**45613**	**7.999**	**0.011**	*
Thickness	1	680	680	0.119	0.734	
Speed	1	3488	3488	0.611	0.444	
Temperature:Thickness	1	15046	15046	2.638	0.122	
Temperature:Speed	**1**	**22662**	**22662**	**3.974**	**0.0625**	**.**
Thickness:Speed	1	14459	14459	2.535	0.129	
Residuals	17	96937	5702			

Signif. codes: 0 ‘***’ 0.001 ‘**’ 0.01 ‘*’ 0.05 ‘.’ 0.1 ‘ ’ 1

The parameter which plays the most relevant role, and which affects all the mechanical properties under consideration is the interaction between printing speed and nozzle temperature. It is the only parameter which influences components tensile modulus. Its p-value falls slightly out of the fixed range < 0.05, i.e., 5 %, in the case of flexural strength, but considering that it is equal to 6.25 %, it is reasonable to assume its importance even for this mechanical property. Temperature is the second most relevant parameter, and it plays the predominant role in defining Ti6Al4V components flexural performance. As for printing speed and nozzle temperature interaction, its p-value falls slightly out of the fixed range < 0.05, i.e., 5 %, in the case of flexural strength, but considering that it is equal to 7.9 %, it is again reasonable to assume it as an important parameter even for this mechanical property. Layer thickness is not crucial when modified between 200 and 300 μm highlighting its statistical significance of 3.5 % only for tensile strength.

In light of the results obtained, the response surface analysis to optimize Ti6Al4V mechanical performance as a function of the 3D printing parameters was carried out using a linear function which only considered nozzle temperature, printing speed and their interaction. A linear function was selected because a two-level DoE was applied and the results obtained are reported in Figure 2.

For all mechanical properties under consideration, the best performance is always obtained with the same printing configuration, i.e., a 160 °C nozzle temperature and a 15 mm/s printing speed. This can be likely ascribed to the improved flowability of the polymeric binder at higher nozzle temperatures combined with a lower printing speed which allows to prevent dragging phenomena. The response surfaces analysis not only allows to identify the optimal manufacturing conditions, but it also allows to draw some further and important conclusions. In particular, it can be observed that the printing configuration opposite to the optimal one, i.e., 140 °C nozzle temperature and 25 mm/s printing speed, does not result in the worst mechanical performance. Indeed, the poorest performance is obtained with the 140 °C-15 mm/s and 160 °C-25 mm/s configurations. In particular, using the optimal nozzle temperature of 160 °C, but an excessively high printing speed, i.e., 25 mm/s, the extruded material becomes extremely fluid, but it does not have enough time to settle, thus experiencing dragging phenomena which prevent a good adhesion between adjacent layers. By using the optimal printing speed of 15 mm/s, but the lower nozzle temperature of 140 °C, the material is extruded at a lower temperature and it is also deposited on a substrate which has undergone an excessive cooling due to the lower printing speed thus leading again to adhesion issues between adjacent layers. In this perspective, the 140 °C- 25 mm/s configuration performs better than the latter two because the higher printing speed ensures that the material is deposited more quickly, thus counteracting the excessive undercooling of the substrate while the reduced extrusion temperature of the polymeric material allows to prevent dragging phenomena. This promotes a satisfying adhesion between adjacent layers although it is not yet comparable with the optimum one. All the aforementioned phenomena were already reported in previous studies performed on pure polymeric filaments, i.e., polylactic acid (PLA), 3D printed by FDM [35,36]. However, microstructural and morphological characterization of the specimens were performed to further corroborate these findings.

Before unveiling the effect of microstructure and morphology on Ti6Al4V components mechanical response, it is fundamental to highlight that the optimum mechanical properties obtained in the present work are much higher than the ones reported in previous works for this type of alloy manufactured by BMD, and are perfectly comparable with the ones achievable through MIM. In particular, a tensile strength of 915 MPa was reached in the present work which is significantly higher than the 750 MPa reported by Eickhoff et al. [37] and by Bragaglia et al. [24] and the 875 MPa reported by Singh et al. [28] for Ti6Al4V components manufactured by BMD. Focusing on MIM manufacturing, the results obtained are still excellent considering that Ergul et al. [38] reported a 704 MPa, Ferri et al. a 800 MPa [39], Shibo et al. a 835 MPa [40], Obasi et al. a 860 MPa [41] and Nor et al. [42] a 934 MPa tensile strength for Ti6Al4V parts produced by MIM. Finally, the results are still promising when compared with EBM ones considering that Edwards et al. [43] reported a tensile strength of 850 MPa and Chastand et al. [44] a 1045 MPa tensile strength after machining.

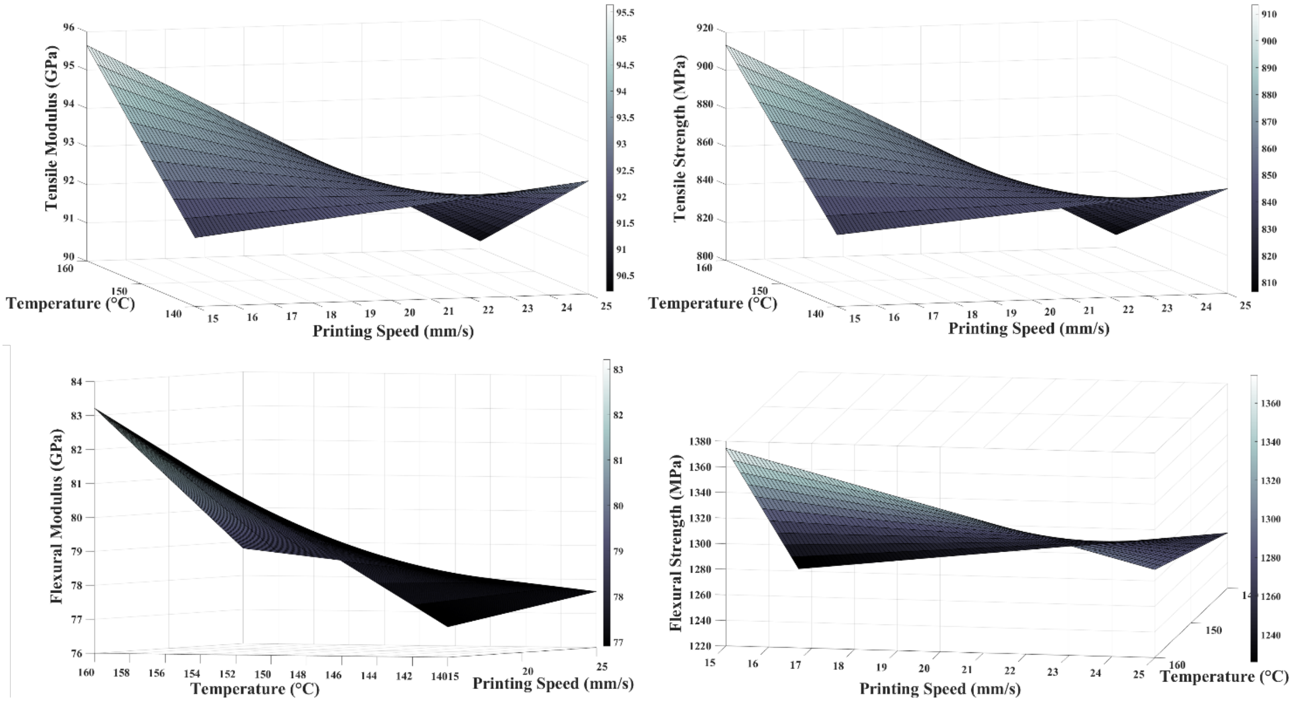

Figure 2: Response surfaces as a function of nozzle temperature and printing speed for tensile modulus and strength and for flexural modulus and strength.

3.2 Microstructural characterization: grain size, XRD

Microstructural and morphological characterizations were carried out to identify the features and the factors responsible for the different mechanical responses of the configurations under consideration. An equiaxed grain structure was observed for all specimens, and Figure 3 shows the grains diameters distributions of the eight 3D printed families. No significant variations can be observed, with average diameter values ranging from 15.4 to 19.7 µm. These variations in diameter can be considered negligible because they would induce a change of only 7 MPa in Ti6Al4V yield stress calculated with the Hall-Petch equation and using the constant parameters σ_0 and k_s provided by Chong et al. [45] for a fully equiaxed Ti6Al4V alloy. This constancy in grains size among the different configurations can be ascribed to the fact that all specimens were sintered in the same conditions, and this is the controlling manufacturing step when dealing with grain growth.

Despite the change in grains diameter can be considered negligible in terms of effect on Ti6Al4V mechanical properties, it can be pointed out that, being equal the nozzle temperature and the printing speed, an increase in layer thickness determines a slight decrease in the average grain diameter, i.e., C1>C3, C2>C4, C5>C7, C6>C8. Similar findings were reported by Tosto et al. [26] for 316L stainless steel ascribing the trend to the higher number of discontinuities resulting from the layer thickness reduction, which entails a higher surface area and free energy for the system. Indeed, a higher particle coalescence is supposed to be required to close the discontinuities and reach metal densification thus resulting in an increase in average grain diameters.

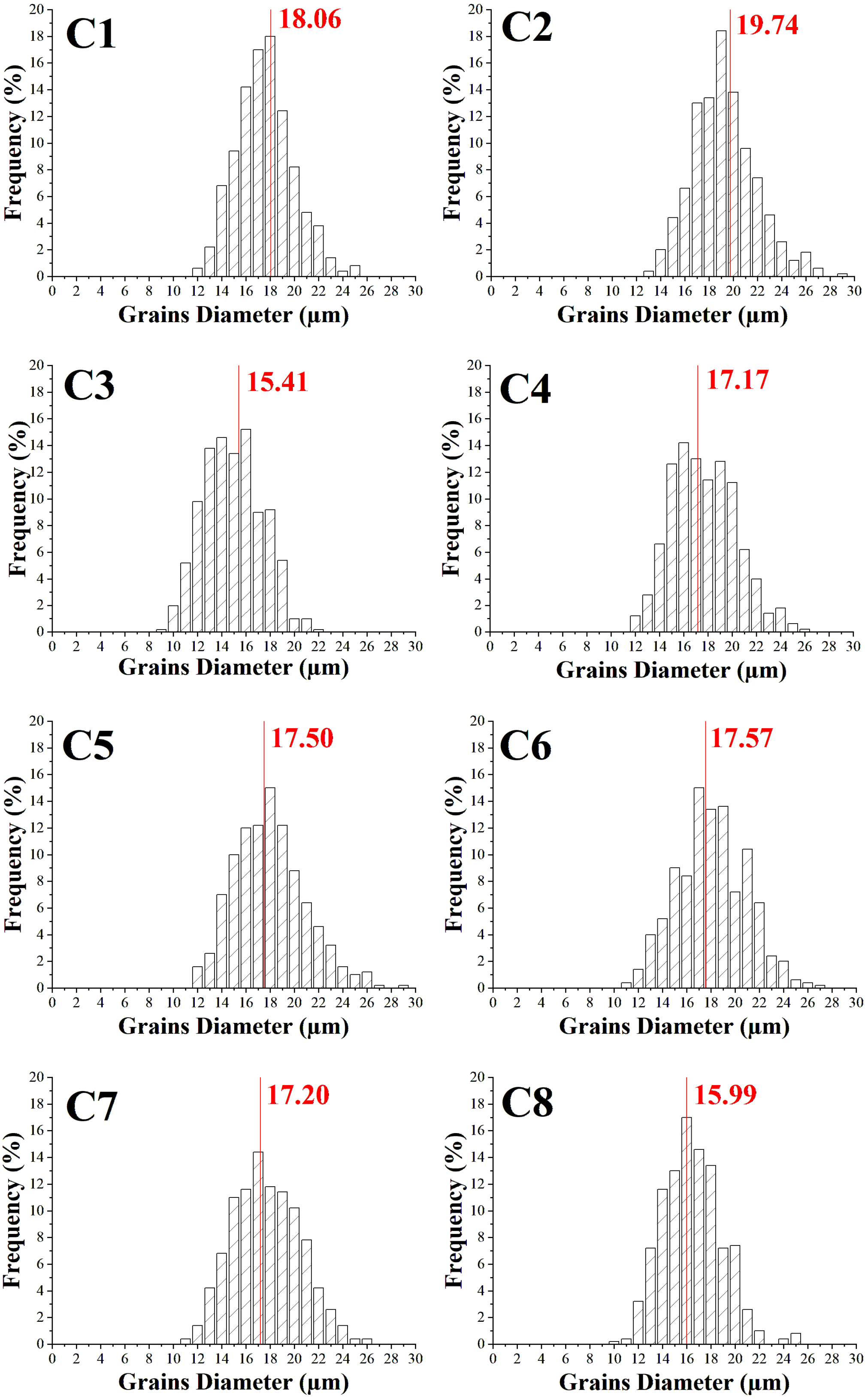

Figure 3: Grain size distributions of the eight different printing configurations.

Figure 4 reports the X-ray diffractograms of each 3D printing configurations, and again, no significant differences were observed among the specimens in terms of phases and distribution as also confirmed by the EBSD analysis reported in section 3.4 for the C4 and C8 configurations. This must be again ascribed to the debinding and sintering processes which are common to all specimens, thus ensuring the same thermal history. All specimens are characterized by a main alpha phase, which makes up the main body of the equiaxed grain, and by a secondary beta phase which is mainly segregated at the grain boundaries, as evidenced by EBSD analyses. The typical diffraction peaks corresponding to the (100), (002), (101), (102), (110), (103), (112) and (201) planes of the alpha phase can be observed at 35.5°, 38.5°, 40.5°, 53.4°, 63.6°, 71.0°, 76.9° and 78.2°, respectively [46]. Moreover, the beta phase peaks resulting from the (110) plane and the (200) plane can be observed at 39.8° and 57.7°, respectively [46].

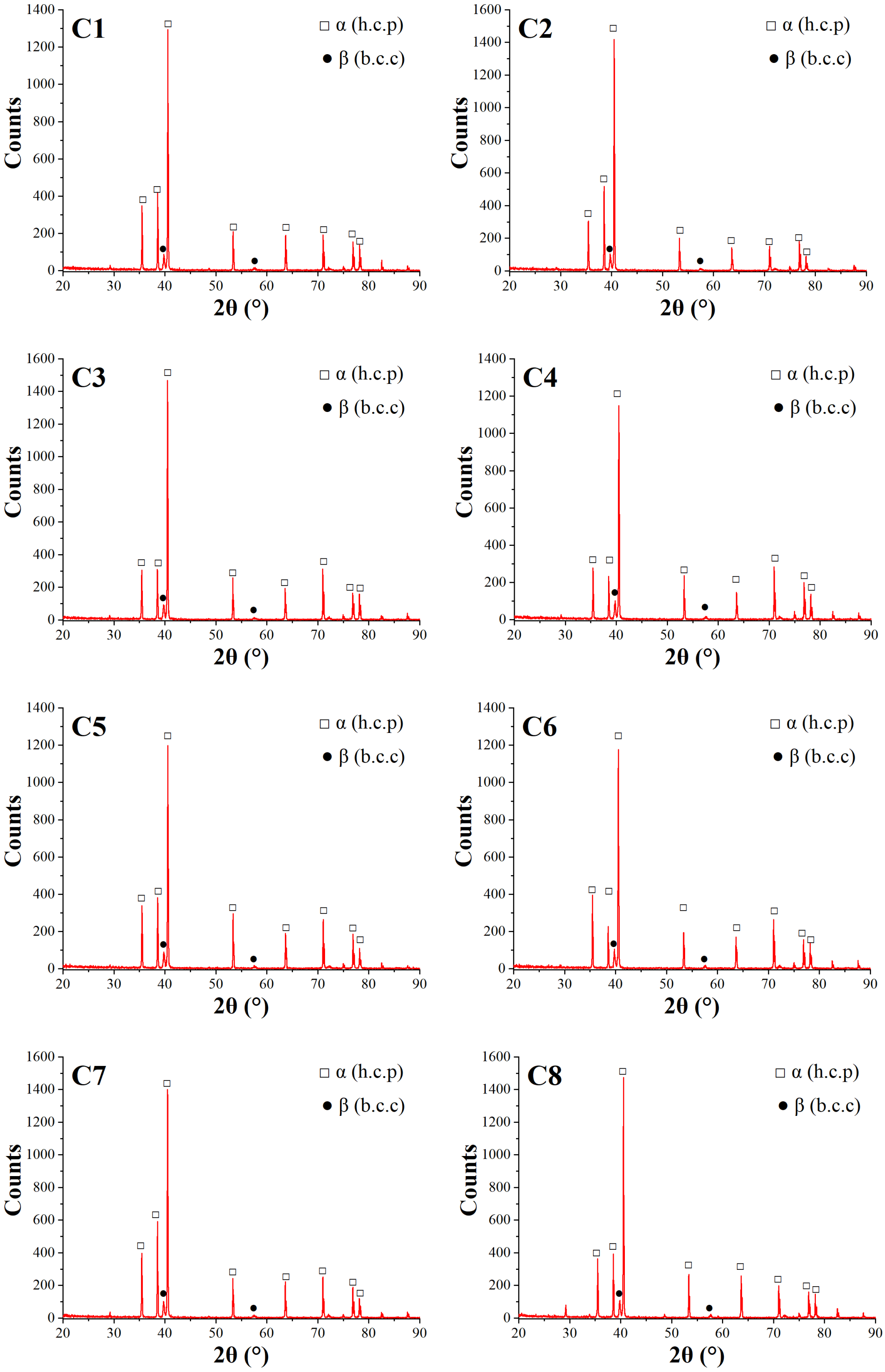

Figure 4: X-Ray diffractograms of the eight different printing configurations.

3.3 Micro CT

Microstructural characterization of grain sizes and phase composition did not disclose any significant differences between the eight 3D printed configurations, therefore micro-CT analysis was exploited to further characterize specimens from a morphological perspective and to point out the main features responsible for their different mechanical response. In particular, Table 6 summarizes the porosity and density values obtained for each configuration. The worst mechanical performance observed from the surface response analysis for configurations C2-C4 and C5-C7, i.e., the ones printed with 140 °C- 15 mm/s and 160 °C- 25 mm/s respectively, are confirmed by the micro-CT analysis which highlighted a porosity higher than 10 % for all of them.

Concerning C5 and C7, the hypothesis of the poor adhesion resulting from dragging phenomena induced by the low viscosity of the extruded material, which does not have enough time to settle, seems to be confirmed as two types of porosities were found to coexist in the sample, as shown in Figure 5 for both 200 and 300 µm layer thickness. In particular, the first type of porosity is connected with the deposition path and highlights a lack of material between two parallel adjacent depositions. These pores are characterized by an elongated shape and have been detected in all samples. In contrast, the second type of porosity is detected inside the deposition path (red arrows in Figure 5), thus causing a non-uniform density along it. This second type of pores is more spherical and smaller in size and may be ascribed to "stick-spurt" or helical instability phenomena which determine a non-uniformity of the deposited layer as the shear rate increases [47]. Moreover, a disordered deposition of the polymeric layers was detected as proved by the front and top views shown in Figure 5 which shows a certain inclination of the layers with respect to the build platform.

Table 6: Porosity values evaluated through micro CT in a volume inside the sample of 5 mm × 4 mm × 8 mm.

	Porosity (%)	**Density (%)**
C1	4.61	95.39
C2	N.A.	<90
C3	4.52	95.48
C4	N.A.	<90
C5	N.A.	<90
C6	5.26	94.74
C7	N.A.	<90
C8	6.78	93.22

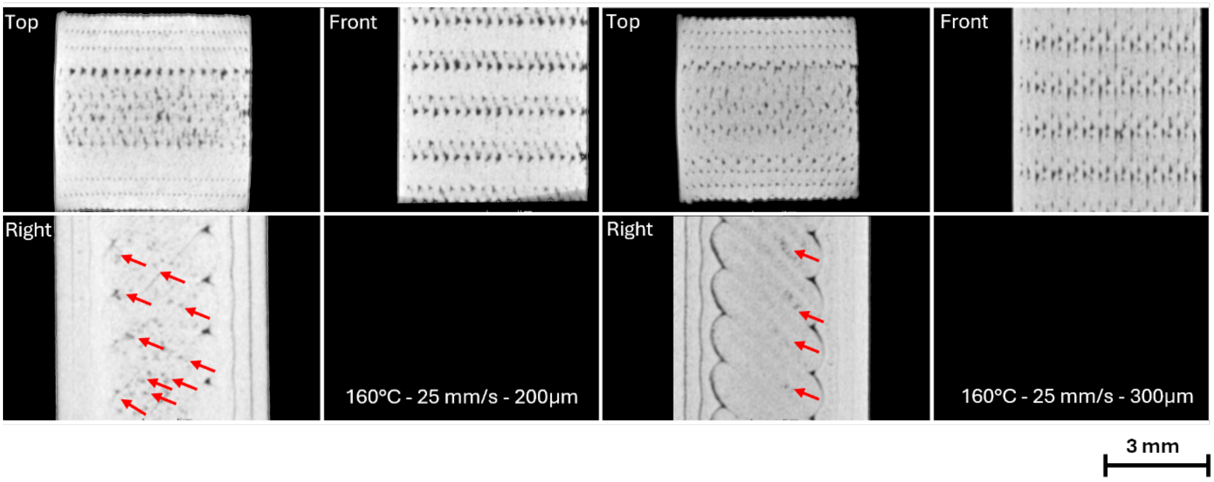

Figure 5: Examples of top, front and right sections obtained through micro-CT of 160 °C-25 mm/s 3D printed samples with 200 and 300 µm layer thickness, respectively.

This disorder in the deposition path can also be observed in the fracture surfaces of these two configurations reported in Figure 6, where the deposited layers do not appear perfectly aligned displaying a small deflection and a certain jagging.

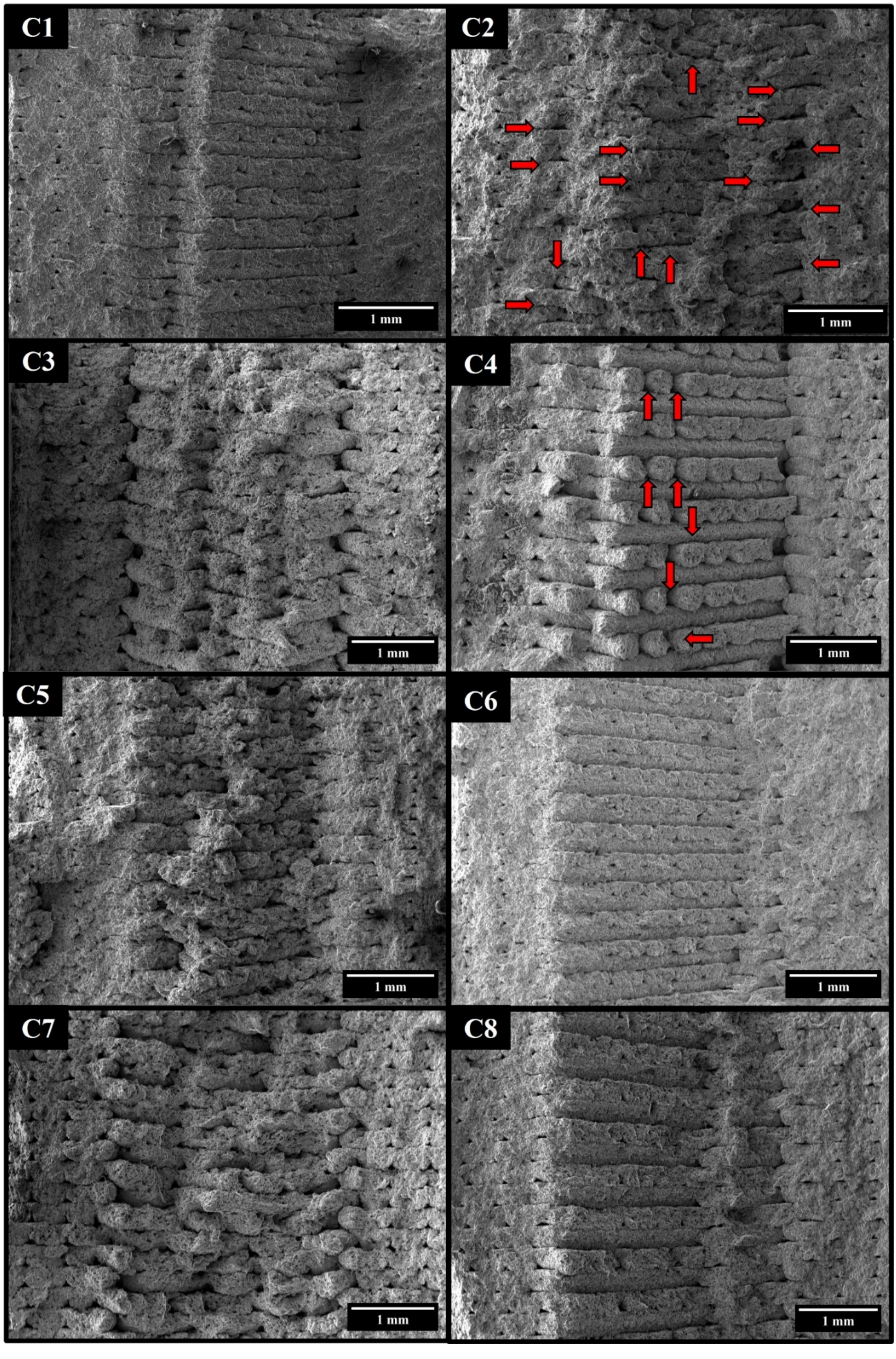

Figure 6: Fracture surfaces of the eight 3D printed configurations subjected to tensile tests.

Concerning configurations C2 and C4, a poor adhesion resulting from the polymeric material being extruded at a lower temperature and on a substrate which underwent excessive cooling due to the lower printing speed was hypothesized. The high porosity values and the SEM micrographs confirm this hypothesis, highlighting strong discontinuities between adjacent layers (red arrows in Figure 6) which can be observed especially for the 300 µm layer thickness configuration. The latter displays perfectly rounded layers which can be easily distinguished one from the other and which are symptomatic of a poor connection between subsequent deposited layers.

Focusing on configurations C1-C3 and C6-C8, all display a porosity between 4.5 and 6.8 % which is slightly higher than the one reported by Shibo et al. [40] which ranges between 2.5 and 5.2 %, and by Obasi et al. [41] which is around 2 % for Ti6Al4V components manufactured by MIM. Despite the slightly higher density reported in the aforementioned works, the higher mechanical properties reported in the present work can be probably ascribed to the lower average grain size which ranges from 15.4 to 19.7 µm and is significantly lower than the 157 µm reported by Obasi et al. [41] and is also lower than the diameter of the powders used in the feedstock by Shibo et al. [40] which ranged between 25 and 45 µm.

Configurations C6-C8 outperform C1-C3, as also confirmed by the surface response analysis, despite exhibiting a slightly higher porosity. These outcomes can be justified by porosity morphology. Indeed, not only the total porosity content but also the shape and geometry of the pores proved to be determinant in defining the mechanical response of metal components. Irregularly shaped pores are typical defects resulting from a lack of fusion [48], a phenomenon highly probable given the sintering process employed in the present work. Such pores act as stress concentrators thus favoring crack nucleation and accelerating crack propagation and reducing material's mechanical performance. However, their effect is highly dependent on their shape. Indeed, Liu et al. [48] reported that spherical pores can result in a more uniform strain distribution thus leading to improved ductility and strength of the metallic samples while Yan et al. [49] demonstrated that samples with a higher pore shape factor, i.e., a shape factor equal to 1 denotes a perfect spherical pore, were also characterized by a higher fatigue endurance limit. Figure 7 reports the sphericity indices of the pores as a function of their diameter for configurations C3 and C8, which are characterized by the same layer thickness, but exhibit the most significant difference in porosity content, i.e., 4.52 % against 6.78 %. Despite its higher porosity, configuration C8 is characterized by a higher pore sphericity with a maximum value of 0.71 for the smallest pores compared to 0.66 of configuration C3, and by an average pore sphericity of 0.47 compared to 0.44 of configuration C3. Moreover, larger pores in configuration C8 display a sphericity of 0.24 whereas those of configuration C3 reach only 0.15. Given that configuration C8 displays a tensile stiffness 2.6 % higher, a tensile strength 8.7 % higher, a flexural stiffness 10.8 % higher and a flexural strength 17.3 % higher than configuration C3, it is undeniable that pores shape plays a crucial role in defining the mechanical response of Ti6Al4V components.

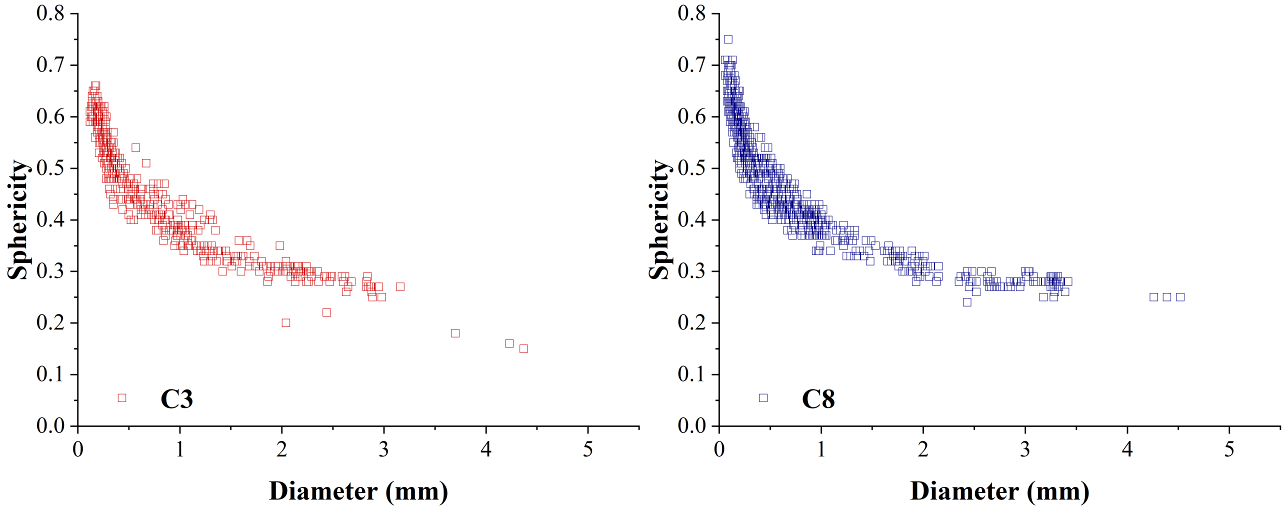

Figure 7: Sphericity indices of pores as a function of their diameter for C3 and C8 configurations

3.4 Nanoindentation and EBSD

In this section, the mechanical characterization workflow and its correlation to microstructural features for printed Ti6Al4V samples are detailed. First, Continuous Stiffness Measurement (CSM) nanoindentation provides average elastic modules and hardness profiles through indentation depth, offering an integrated mechanical response of the samples without spatially resolved microstructural information. Although helpful in assessing overall nanoscale mechanical performance, the CSM approach inherently limits the direct identification of specific microstructural features responsible for observed mechanical behaviors. To address this limitation, high-speed nanoindentation mapping, which enables one complete indentation cycle per second, allowing for high-resolution, spatially resolved mapping of hardness (H) and elastic modulus (E), is subsequently employed. Coupled with Electron Backscatter Diffraction (EBSD) analyses, high-speed mapping allows explicit correlation between localized mechanical properties and specific microstructural attributes, such as grain orientation and phase distribution. Therefore, the sequential application of CSM nanoindentation, high-speed mapping, and EBSD analyses ensures a comprehensive understanding of the microstructure-property relationships in additive-manufactured Ti6Al4V alloys at the nano- and microscale.

Figure 8 shows the results from the CSM nanoindentation analysis of all samples, including the results of elastic modulus (a) and hardness (b) as a function of the indentation depth. Moreover, Figure 8.c summarizes the elastic modulus and hardness values of all configurations under study at 400 nm.

From the elastic modulus perspective, it can be noticed that configurations C6 and C8 are again characterized by the highest values, thus confirming to be the optimum configurations as already proved by the response surface analysis. In particular, configuration C6 displays a modulus of 137.2±7.8 GPa at 400 nm while configuration C8 displays a stiffness of 157.9±6.2 GPa at 400 nm. Focusing on the other configurations, an interesting trend can be detected as a function of the layer thickness. This parameter did not display any statistical significance on samples mechanical performance at the macroscopic level, but proved to be an essential factor at the nano level. In particular, configurations C1, C2 and C5 which are characterized by a layer thickness of 200 μm exhibit an elastic modulus of 132.5±3.5 GPa, 133.3±4.8 GPa and 130.3±4.2 GPa, respectively, which are almost 13 % higher than the one of the corresponding configurations C3, C4 and C7 characterized by a layer thickness of 300 μm, which exhibit an elastic modulus of 117.7±2.4 GPa, 116.9±4.7 GPa and 1116.6±3.1 GPa, respectively. These outcomes can be justified by recalling the results reported in section 3.2 for the grain sizes, where it was stated that the change in grain diameter was negligible in terms of the macroscopic effect on Ti6Al4V mechanical properties, but a trend as a function of layer thickness being equal nozzle temperature and printing speed was also detected. In particular, it was reported that an increase in layer thickness determined a slight decrease in the average grain diameter which is, in turn, responsible for an increase in grain boundary extent. As will be demonstrated by the following EBSD analysis, the Ti6Al4V beta phase tends to segregate at the grain boundaries and it is characterized by an elastic modulus lower than alpha phase one [50,51]. Therefore, considering the nanoscale level of the test, it becomes statistically more likely to indent the beta phase when grain boundary extension increases.

Focusing on hardness results, it consistently decreased for all configurations due to increasing indentation volume and plastic zone size with depth, progressively integrating softer phases and defects. The results are also coherent with the ones previously obtained with configurations C6, C8, C1, and C3 displaying the highest values ranging from 5.2 to 5.6 GPa and configurations C2, C4, C5 and C7 displaying the lowest values ranging from 3.9 to 5.2 GPa. Putting all results together, it can be concluded that sample C8 is the best choice when evaluating the combination of elastic modulus and hardness, offering a balance of stiffness and resistance to permanent plastic deformation. In contrast, sample C4 consistently underperformed in this combined metric. From the above-mentioned results,, samples C8 and C4 were selected for further analysis through high-speed nanoindentation mapping, considering that they are also characterized by the same layer thickness. Additionally, EBSD analysis conducted on samples C4 and C8 provided crucial microstructural insights to interpret high-speed indentation results, especially by clarifying grain morphology and phase distribution relationships.

Figure 9 shows the grains shape aspect ratio of both C4 and C8 configurations calculated as the ratio of the minor axis length to the major axis length of an ellipse fitted to an irregular grain and the related low magnification grains maps. The results obtained confirmed the equiaxed nature of the grains, considering that they are usually recognized as equiaxed when their average aspect ratio ranges between 0.4 and 1 [52] and configurations C4 and C8 are characterized by an average aspect ratio of around 0.6 for both configurations. Figure 10 reports the maps of grains orientation maps along the x, y and z axes for C4 and C8 and highlights an important outcome, i.e., the random orientation of the crystalline planes, which will be fundamental to explain the high-speed nanoindentation maps results. Finally, Figure 11 allows to evaluate the distribution and the amount of the alpha and beta phases throughout the samples. In particular, both configurations display a significant segregation of the beta phase at the grain boundary, as heralded in the previous paragraphs, and its content is comparable and equal to 5.5 % for C4 and to 4.2 % for C8. This phase distribution data is crucial, as differences in the proportion and localization of β-phase at grain boundaries directly affect the local mechanical responses observed in the nanoindentation maps. In particular, the β-phase's lower mechanical properties significantly influence nanoindentation outcomes at higher grain boundary densities.

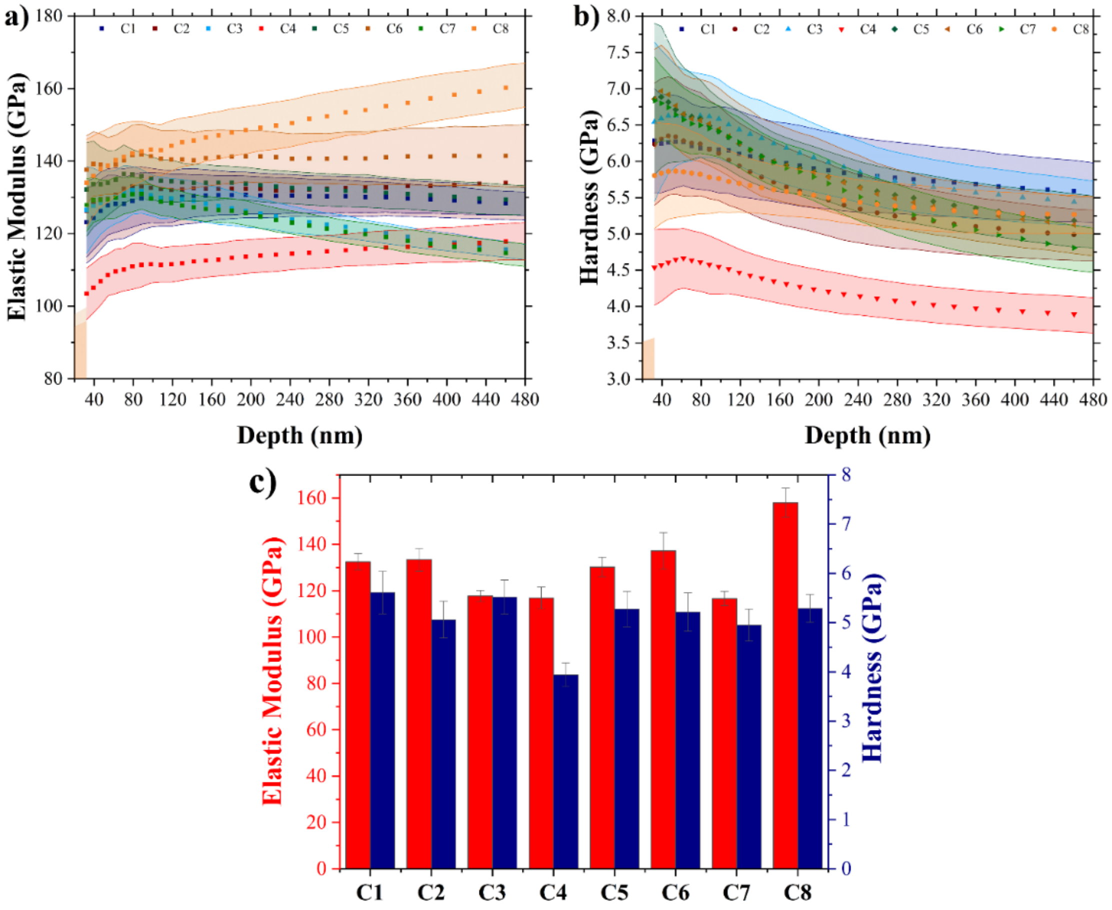

Figure 8: CSM nanoindentation curves for the elastic modulus and hardness (a,b) and average values of elastic modulus and hardness at an indentation depth of 400 nm with error bars representing the standard deviation (c).

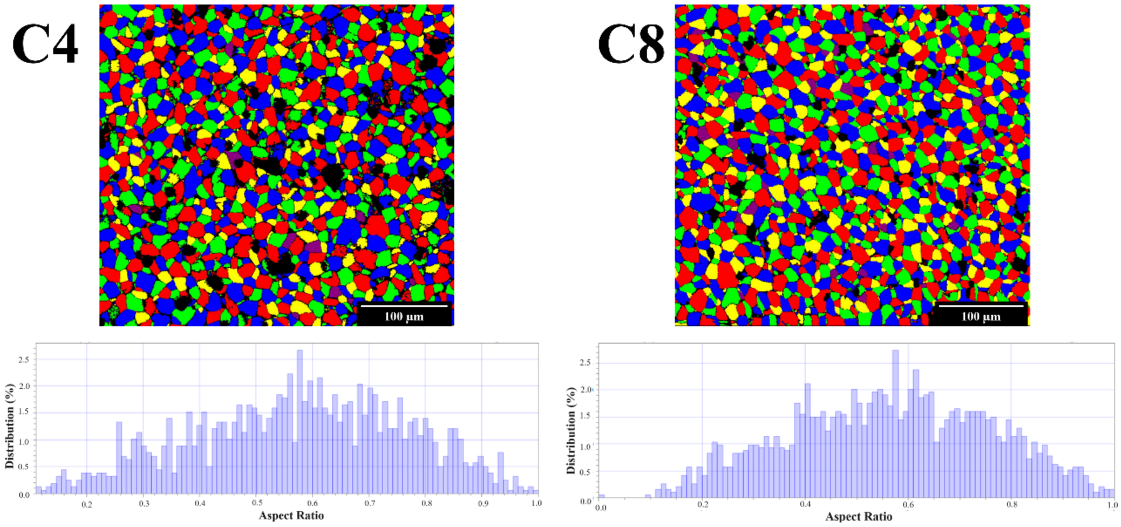

Figure 9: Grains map and grains shape aspect ratio for both C4 and C8 configurations obtained from the low magnification map.

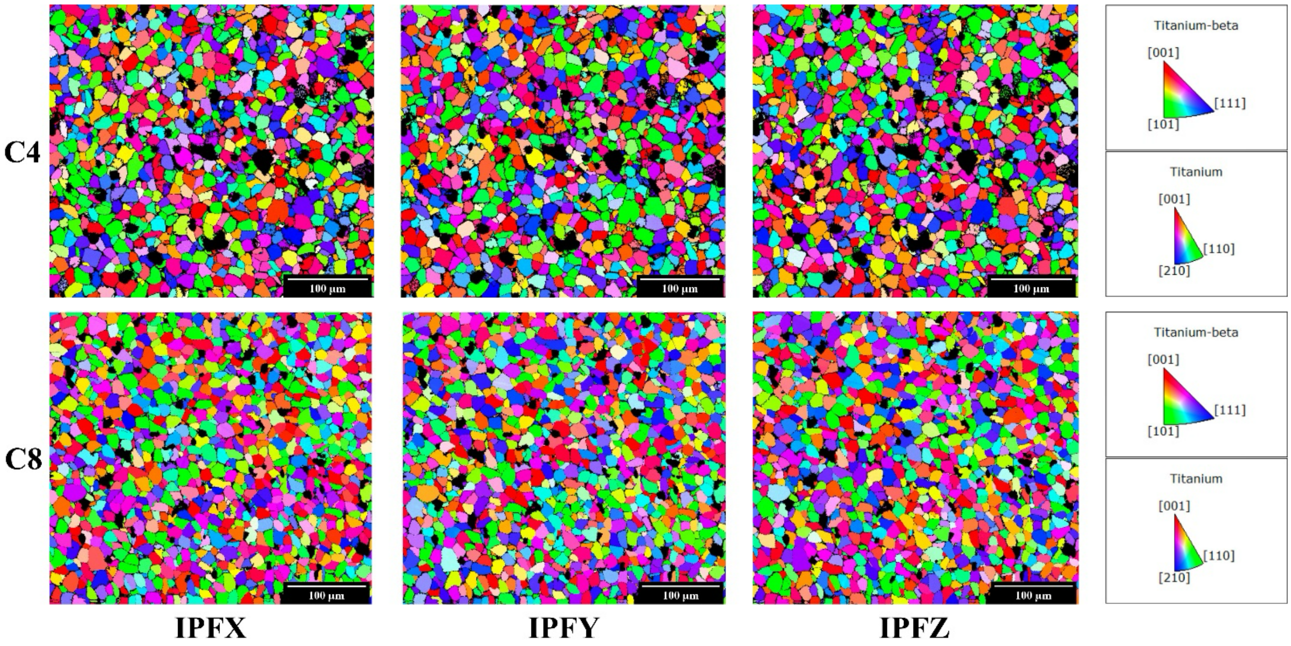

Figure 10: Grain orientation maps along the x (IPFX), y (IPFY) and z (IPFZ) axes for both C4 and C8 configurations obtained from the low magnification map.

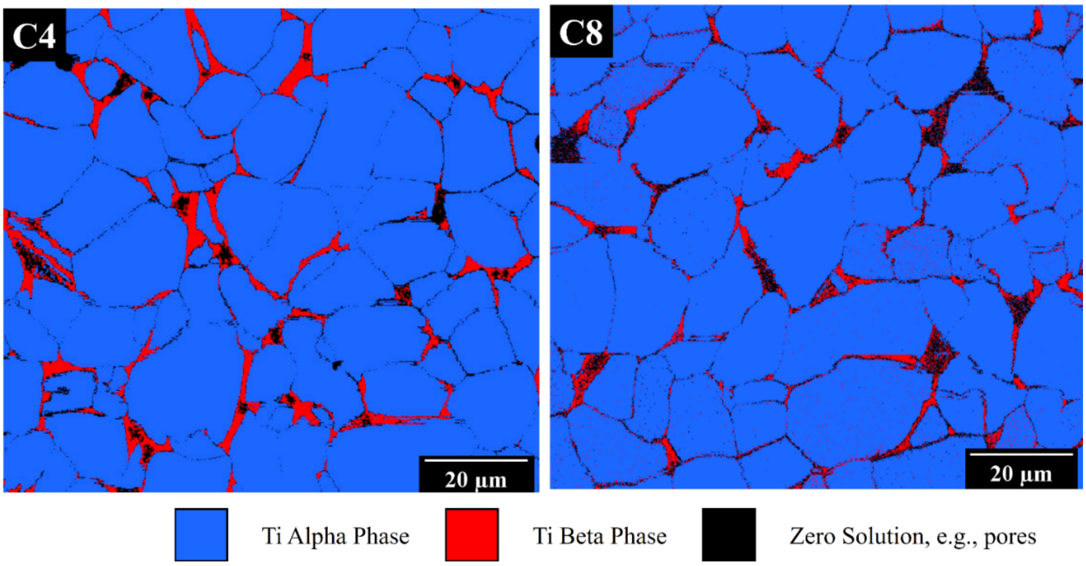

Figure 11: Alpha and beta phases distribution in both C4 and C8 configurations obtained from the high magnification map.

High-speed nanoindentation mapping results are illustrated in **Errore. L'origine riferimento non è stata trovata.** (left side) and they present a first qualitative interpretation of the mechanical properties – microstructure features across the two samples in terms of spatially-resolved elastic modulus and hardness. Significant differences can be recognized between samples C4 and C8, with C8 being characterized by a pronounced prevalence of harder phases. These hardness differences are directly correlated to local microstructural heterogeneities, which were clearly identified through EBSD analysis. Specifically, the spatial resolution of high-speed nanoindentation highlights the heterogeneous nature of additively manufactured alloys, revealing how specific microstructural features, such as phase distributions, grain boundaries, and local crystallographic orientations, influence the local mechanical behavior. These preliminary insights are foundational to the detailed examinations conducted via 1D and 2D Gaussian Mixture Model (GMM) deconvolutions. The mechanical deconvoluted data from 1D GMM and 2D GMM deconvolution protocols showcased the properties of three distinct phases/components. The selection of a three-phase model for deconvolution aligns optimally with the experimental Probability Density Function (PDF) data reported in Figure S3 of Supplementary Materials. The 2D GMM analysis shown in Figure 12 (right side) provides a spatial representation of the three phases, offering insights into how they are distributed throughout the material.

Cluster 3 is associated with the lowest values of elastic modulus and hardness for both C4 and C8, as proved by the data summarized in Tables 7 and 8 and can be ascribed to the beta phase segregated at the grain boundary as confirmed by the EBSD analysis. Nevertheless, it is likely that cluster 3 also includes some defects such as micropores, considering that it covers a higher amount of data in sample C4, i.e., the ones characterized by the worst mechanical properties, and that beta phase content is comparable between C4 and C8. This interpretation aligns with EBSD findings, where a similar β-phase fraction, i.e., 5.5 % for C4 and 4.2 % for C8, was detected. Yet, the significantly lower mechanical performance of C4 suggests an increased presence of micropores or other microstructural defects, confirmed indirectly through the nanoindentation-derived cluster analysis. Hence, EBSD and high-speed nanoindentation results reinforce each other, illustrating the apparent interplay between phase segregation, grain-boundary density, and defect presence on mechanical properties.

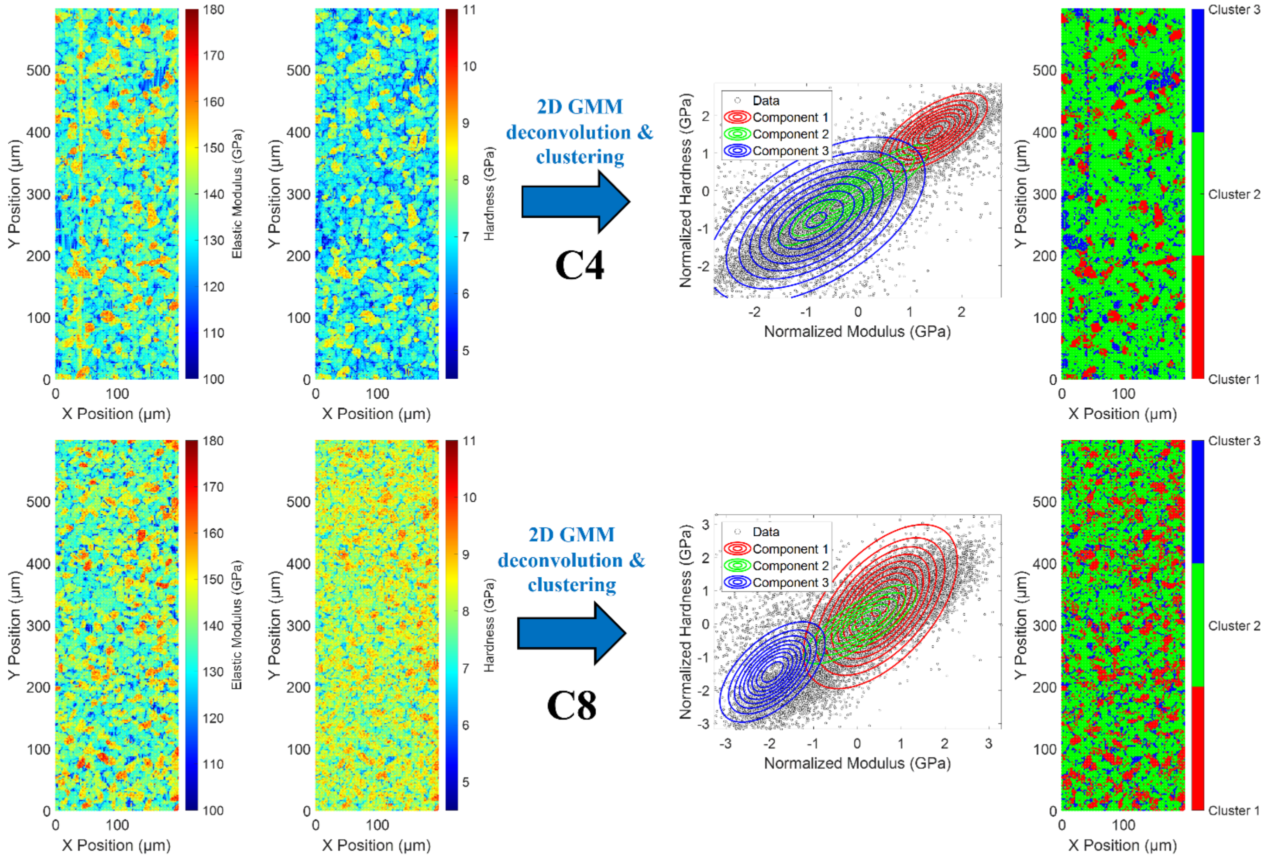

Figure 12: High-speed nanoindentation maps of the elastic modulus and hardness for C4 and C8 configurations and 2D GMM clustering evidencing the three distinct mechanical phases across the nanoindentation map obtained due to the deconvolution procedure.

Focusing on cluster 1, its shapes perfectly recall the ones of some isolated grains and this allows to conclude that both clusters 1 and 2 can be correlated to the alpha phase but with a different grains orientation. Indeed, Kwon et al. [53] reported that in a hexagonal unit cell the basal, prismatic, and pyramidal directions are characterized by different values of hardness and modulus. In particular, the basal orientation is characterized by a 7.7±0.2 GPa hardness and 180.6±2.9 GPa elastic modulus, the prismatic orientation by 5.1±0.1 GPa hardness and a 155.1±2.4 GPa elastic modulus and the pyramidal orientation by a 4.6±0.1 GPa hardness and a 150.5±1.6 GPa elastic modulus. Therefore, it can be concluded that compared to the basal orientation all other relevant directions are less hard and rigid. Similar conclusions were reported by Zambaldi et al. [54] who pointed out the hardness anisotropy of α-Ti by conducting nanoindentation tests on different crystallographic planes. Therefore, grain orientation maps obtained by EBSD are essential for interpreting high-speed nanoindentation results, enabling clear differentiation between mechanically distinct α-phase grains based on their crystallographic orientations. Overall, integrating CSM nanoindentation, high-speed mapping, and EBSD analyses enabled a clear and explicit correlation of local mechanical responses to specific microstructural characteristics, addressing the complexities inherent in additively manufactured Ti6Al4V samples.

Table 7: Mechanical deconvolution data of C4 configuration obtained through 1D GMM deconvolution and 2D GMM clustering techniques for the three identified populations/clusters. The percentage of data coverage is also provided.

Cluster	1D GMM Elastic Modulus (GPa)	1D GMM Hardness (GPa)	2D GMM Elastic Modulus (GPa)	2D GMM Hardness (GPa)	Data Coverage (%)
1	148.5± 7.3	8.17±0.47	154.1± 4.4	8.43± 0.37	14.16
2	133.6±5.3	6.98±0.45	134.4± 6.9	7.01± 0.59	74.29
3	118.6± 5.9	5.75±0.43	124.1± 12.4	6.14± 0.88	11.54

Table 8: Mechanical deconvolution data of C8 configuration obtained through 1D GMM deconvolution and 2D GMM clustering techniques for the three identified populations/clusters. The percentage of data coverage is also provided.

Cluster	1D GMM Elastic Modulus (GPa)	1D GMM Hardness (GPa)	2D GMM Elastic Modulus (GPa)	2D GMM Hardness (GPa)	Data Coverage (%)
1	144.9± 9.6	8.26±0.46	148.8± 14.5	8.65± 0.62	20.93
2	136.1±4.8	8.16±0.71	138.7± 6.4	8.14± 0.47	68.34
3	120.5± 7.8	6.53±0.39	121.8± 7.6	6.56± 0.35	10.73

3.5 Multi-scale correlation of mechanical properties

The integration of results from nanoindentation and electron backscatter diffraction (EBSD) analyses significantly enhances the detailed interpretation of macro-scale mechanical properties derived from response surface analysis. The response surface analysis in Figure 2 has identified configurations C6 and C8, manufactured with a nozzle temperature of 160 °C and a printing speed of 15 mm/s, as optimal configurations. In particular, they exhibit a tensile strength of 915 MPa which is markedly higher than the 802 MPa of configuration C4. These results indicate that the optimal printing conditions lead to effective polymer flow, uniform deposition, and strong interlayer adhesion, which are essential for enhanced mechanical performance. At the nanoscale, the Continuous Stiffness Measurement (CSM) nanoindentation results reported in Figure 8c reaffirmed these trends revealing that configurations C6 and C8 achieved the highest elastic moduli, i.e, 137.2 ± 7.8 GPa and 157.9 ± 6.2 GPa, as well as substantial hardness values, i.e., 5.6 ± 0.4 GPa and 5.5 ± 0.3 GPa. A consistent relationship concerning layer thickness was observed, noting that configurations with thinner layers of 200 μm demonstrated elastic modulus values roughly 13% higher (ranging from 130 to 133 GPa) than those of thicker layers of 300 μm (values from 111 to 118 GPa). While this trend is statistically insignificant in terms of macro-scale properties, it highlights critical microstructural influences that can be detected at the nanoscale. EBSD analyses supported this observation by revealing that thicker layers had a reduced grain diameter, i.e., 15.4–17 μm for 300 μm layers in contrast to 18–19 μm for 200 μm layers, which consequently increased grain boundary density thus increasing the likelihood of encountering softer β-phases at grain boundaries, thereby leading to decreased local mechanical properties.

High-speed nanoindentation mapping further clarified the relationships between microstructure and mechanical properties thanks to an extensive examination of samples C4 and C8 which were characterized by the same layer thickness but significantly distinct macro-scale properties. The enhanced legibility and analysis of high-speed indentation maps reported in Figure 12 allowed the identification of three mechanical clusters through Gaussian Mixture Model (GMM) analysis. Notably, Cluster 3, which comprised the mechanically softer β-phase and micropores, constituted a larger data fraction in configuration C4 (11.54%) than in configuration C8 (10.73%). This subtle difference in cluster distribution significantly influences macro-scale properties, thereby explaining the inferior mechanical response of C4.

Moreover, EBSD analyses confirmed that Clusters 1 and 2 are predominantly associated with α-phase grains, characterized by diverse crystallographic orientations. Previous studies have highlighted significant anisotropy in mechanical properties, indicating that basal orientations exhibit elastic modulus values around 180 GPa and hardness of 7.7 GPa, substantially exceeding those of prismatic or pyramidal orientations with elastic moduli of about 150–155 GPa and hardness values around 4.6–5.1 GPa.

In summary, this multiscale characterization provides clear evidence that the optimized printing parameters identified through macro-scale analyses are directly linked to beneficial microstructural features and improved local mechanical properties, culminating in enhanced overall mechanical performance.

4 CONCLUSIONS

Thanks to high specific mechanical properties and excellent corrosion resistance, the Ti6Al4V alloy is widely used in industrial applications. Still, despite all its advantages, few works focused on the optimization of the BMD process for this alloy and none of them investigated the optimization of the 3D printing parameters which is a crucial aspect to reduce the presence of voids between adjacent layers. In light of this, the present work tried to bridge this gap of knowledge by investigating the effect of three fundamental printing parameters, i.e., layer thickness, nozzle temperature and, printing speed, and optimizing the 3D printing process by exploiting the DoE and surface response analysis techniques. The results obtained are extremely auspicious considering that the optimum configurations, i.e., C6 and C8, displayed a tensile strength of 915 MPa which is perfectly comparable to MIM components.

The statistical analysis demonstrated that nozzle temperature and printing speed, and in particular their interaction, are the most affecting parameters and that the 3D printing optimum is achieved with a nozzle temperature of 160 °C, i.e., the high-level value, in conjunction with a printing speed of 15 mm/s, i.e., the low-level value. This condition is the best compromise to ensure a good flowability of the polymeric binder while preventing dragging phenomena. The results obtained with tensile and flexural tests were also confirmed by the nanoindentation tests which highlighted the superiority of configurations C8.

The morphological characterization did not disclose significant differences among the different configurations in terms of phases, amount, and disposition nor of average grains size, but pointed out significant differences in terms of porosity amount and shape. In particular, the optimum configurations are characterized by an average porosity of 5.3-6.8 %, which is significantly lower than the one of the worst configurations (C2, C4, C5 and C7), but is slightly higher than the one of intermediate configurations C1 and C3 characterized by a porosity of around 4.5 %. In this case, the higher sphericity of porosity allows to counterbalance the slightly higher content making the defect less critical.

Competing Interests: The authors declare no conflicts of interest.

Acknowledgements

This work was supported by the European Union - NextGenerationEU (National Sustainable Mobility Center CN00000023, Italian Ministry of University and Research Decree n. 1033 - 17/06/2022, Spoke 11 - Innovative Materials & Lightweighting). The authors also acknowledge the Integrated Additive Manufacturing Center (IAM) at Politecnico di Torino, Torino, Italy, where the X-ray Computed Tomography measurements and analyses have been performed. E. Rossi and M. Sebastiani gratefully acknowledge partial financial support from the national project, PRIN 2020 Multiscale modelling/characterization and fabrication of nanocomposite ceramics with improved toughness (CONCERTO), grant agreement no. 2020BN5ZW9.

REFERENCES

[1] A. Aoun, A. Ilinca, M. Ghandour, H. Ibrahim, *Comput. Ind. Eng.* **2021**, *162*, 107746.
[2] R. Lacroix, R. W. Seifert, A. Timonina-Farkas, *Oper. Res. Perspect.* **2021**, *8*, 100201.
[3] T. D. Ngo, A. Kashani, G. Imbalzano, K. T. Q. Nguyen, D. Hui, *Compos. Part B* **2018**, *143*, 172.
[4] J. C. Najmon, S. Raeisi, A. Tovar, in *Addit. Manuf. Aerosp. Ind.*, Elsevier Inc., **2019**, pp. 7–31.
[5] V. Mohanavel, K. S. Ashraff Ali, K. Ranganathan, J. Allen Jeffrey, M. M. Ravikumar, S. Rajkumar, *Mater. Today Proc.* **2021**, *47*, 405.
[6] E. Dalpadulo, A. Petruccioli, F. Gherardini, F. Leali, *J. Manuf. Mater. Process.* **2022**, *6*, 133.
[7] M. Delic, D. R. Eyers, *Int. J. Prod. Econ.* **2020**, *228*, 107689.
[8] M. Leary, *Design For Additive Manufactruing*, Elsevier Inc., Amsterdam, **2019**.
[9] P. C. Priarone, A. R. Catalano, L. Settineri, *Prog. Addit. Manuf.* **2023**, *8*, 1229.
[10] W. E. Frazier, *J. Mater. Eng. Perform.* **2014**, *23*, 1917.
[11] M. Ziaee, N. B. Crane, *Addit. Manuf.* **2019**, *28*, 781.
[12] A. Ilmiah Nurhudan, S. Supriadi, Y. Whulanza, A. S. Saragih, *J. Manuf. Process.* **2021**, *66*, 228.
[13] Formlabs, “3D Printing Technology Comparison: FDM vs. SLA vs. SLS,” can be found under https://formlabs.com/blog/fdm-vs-sla-vs-sls-how-to-choose-the-right-3d-printing-technology/, **2023**.
[14] Markforged, “Types of 3D Printing in Metal,” can be found under https://markforged.com/resources/learn/design-for-additive-manufacturing-metals/metal-additive-manufacturing-introduction/types-of-3d-printing-metal?__geom=✪, **2023**.
[15] A. Mostafaei, A. M. Elliott, J. E. Barnes, F. Li, W. Tan, C. L. Cramer, P. Nandwana, M. Chmielus, *Prog. Mater. Sci.* **2021**, *119*, 100707.
[16] C. Cavallo, “All About Binder Jetting 3D Printing,” can be found under https://www.thomasnet.com/articles/custom-manufacturing-fabricating/all-about-binder-jetting-3d-printing/, **2023**.
[17] Pick3DPrinter, “2023 Best Binder Jetting 3D Printer – Pros and Cons & Buying Guide,” can be found under https://pick3dprinter.com/binder-jetting-3d-printer/, **2023**.
[18] G. F. Bocchini, *SAE Trans.* **1986**, *95*, 790.
[19] S. Spiller, F. Berto, N. Razavi, *Procedia Struct. Integr.* **2022**, *41*, 158.
[20] I. Todd, A. T. Sidambe Dr, in *Adv. Powder Metall. Prop. Process. Appl.*, Woodhead Publishing Series In Metals And Surface Engineering, **2013**, pp. 109–146.
[21] M. Bram Dr, T. Ebel Dr, M. Wolff, A. P. Cysne Barbosa Dr, N. Tuncer Dr, in *Adv. Powder Metall. Prop. Process. Appl.*, Woodhead Publishing Series In Metals And Surface Engineering, **2013**, pp. 520–554.
[22] D. F. Heaney, C. D. Greene, in *Handb. Met. Inject. Molding*, Woodhead Publishing Series In Metals And Surface Engineering, **2012**, pp. 109–132.
[23] T. Ebel, in *Titan. Med. Dent. Appl.*, Woodhead Publishing Series In Biomaterials, **2018**, pp. 531–551.
[24] M. Bragaglia, M. Mariani, C. Sergi, F. Sarasini, J. Tirillò, F. Nanni, *J. Mater. Res. Technol.* **2023**, *27*, 168.
[25] C. Suwanpreecha, A. Manonukul, *Metals (Basel).* **2022**, *12*, 429.
[26] C. Tosto, J. Tirillò, F. Sarasini, C. Sergi, G. Cicala, *Polymers (Basel).* **2022**, *14*, 1.
[27] P. Pushp, S. M. Dasharath, C. Arati, *Mater. Today Proc.* **2022**, *54*, 537.
[28] P. Singh, V. K. Balla, A. Gokce, S. V. Atre, K. H. Kate, *Prog. Addit. Manuf.* **2021**, *6*, 593.
[29] R. Eickhoff, S. Antusch, D. Nötzel, T. Hanemann, *Materials (Basel).* **2023**, *16*, 3162.
[30] Y. Zhang, S. Bai, M. Riede, E. Garratt, A. Roch, *Addit. Manuf.* **2020**, *34*, 101256.
[31] M. K. Dunstana, J. D. Paramore, B. G. Butler, Z. Z. Fang, in *MATEC Web Conf. 14th World Conf. Titan.*, **2020**, p. 03003.
[32] U. VIEHÖFER, W. WINKELMÜLLER, M. LANG, M. SCHARVOGEL, *EP 3 231 536 A1*, **2017**.
[33] E. Rossi, J. M. Wheeler, M. Sebastiani, *Curr. Opin. Solid State Mater. Sci.* **2023**, *27*, 101107.
[34] Z. Zhang, J. Qin, Z. Ma, X. Pang, Y. Zhou, *Cem. Concr. Compos.* **2023**, *138*, 104990.
[35] A. A. Ansari, M. Kamil, *Mater. Today Proc.* **2021**, *45*, 5462.
[36] L. Aliotta, C. Sergi, B. Dal Pont, M. B. Coltelli, V. Gigante, A. Lazzeri, *Mater. Today Sustain.* **2024**,

26, 100780.
[37] R. Eickhoff, S. Antusch, S. Baumgärtner, D. Nötzel, T. Hanemann, *Materials (Basel).* **2022**, *15*, 6442.
[38] E. Ergül, H. Özkan Gülsoy, V. Günay, *Powder Metall.* **2009**, *52*, 65.
[39] O. M. Ferri, T. Ebel, R. Bormann, *Mater. Sci. Eng. A* **2009**, *504*, 107.
[40] G. Shibo, Q. Xuanhui, H. Xinbo, Z. Ting, D. Bohua, *J. Mater. Process. Technol.* **2006**, *173*, 310.
[41] G. C. Obasi, O. M. Ferri, T. Ebel, R. Bormann, *Mater. Sci. Eng. A* **2010**, *527*, 3929.
[42] N. H. M. Nor, N. Muhamad, A. K. A. M. Ihsan, K. R. Jamaludin, *Procedia Eng.* **2013**, *68*, 359.
[43] P. Edwards, A. O'Conner, M. Ramulu, *J. Manuf. Sci. Eng.* **2013**, *135*, 1.
[44] V. Chastand, P. Quaegebeur, W. Maia, E. Charkaluk, *Mater. Charact.* **2018**, *143*, 76.
[45] Y. Chong, G. Deng, S. Gao, J. Yi, A. Shibata, N. Tsuji, *Scr. Mater.* **2019**, *172*, 77.
[46] S. L. R. Da Silva, L. O. Kerber, L. Amaral, C. A. Dos Santos, *Surf. Coatings Technol.* **1999**, *116–119*, 342.
[47] J. F. Agassant, D. R. Arda, C. Combeaud, A. Merten, H. Münstedt, M. R. Mackley, L. Robert, B. Vergnes, *Int. Polym. Process. XXI* **2006**, *21*, 239.
[48] W. Liu, C. Chen, S. Shuai, R. Zhao, L. Liu, X. Wang, T. Hu, W. Xuan, C. Li, J. Yu, J. Wang, Z. Ren, *Mater. Sci. Eng. A* **2020**, *797*, 139981.
[49] Y. Yan, G. L. Nash, P. Nash, *Int. J. Fatigue* **2013**, *55*, 81.
[50] N. Dumontet, D. Connétable, B. Malard, B. Viguier, *Scr. Mater.* **2019**, *167*, 115.
[51] E. A. Trofimov, R. Y. Lutfullin, R. M. Kashaev, *Lett. Mater.* **2015**, *5*, 67.
[52] V. B. Biscuola, M. A. Martorano, *Metall. Mater. Trans. A Phys. Metall. Mater. Sci.* **2008**, *39A*, 2885.
[53] J. Kwon, M. C. Brandes, P. Sudharshan Phani, A. P. Pilchak, Y. F. Gao, E. P. George, G. M. Pharr, M. J. Mills, *Acta Mater.* **2013**, *61*, 4743.
[54] C. Zambaldi, Y. Yang, T. R. Bieler, D. Raabe, *J. Mater. Res.* **2012**, *27*, 356.